Title
On the chemical state of Co oxide electrocatalysts during alkaline water splitting

Journal
Physical Chemistry Chemical Physics, 15(40)

ISSN
1463-9076

Authors
Friebel, Daniel
Bajdich, Michal
Yeo, Boon Siang
et al.

Publication Date
2013

DOI
10.1039/c3cp52981a

Peer reviewed

PCCP

RSC Publishing

PAPER

View Article Online
View Journal | View Issue

Cite this: *Phys. Chem. Chem. Phys.*, 2013, **15**, 17460

On the chemical state of Co oxide electrocatalysts during alkaline water splitting†

Daniel Friebel,*[ab] Michal Bajdich,[ac] Boon Siang Yeo,[c] Mary W. Louie,[ac] Daniel J. Miller,[b] Hernan Sanchez Casalongue,[ab] Felix Mbuga,[b] Tsu-Chien Weng,[d] Dennis Nordlund,[d] Dimosthenis Sokaras,[d] Roberto Alonso-Mori,[e] Alexis T. Bell[ac] and Anders Nilsson[ab]

Received 16th July 2013,
Accepted 5th September 2013

DOI: 10.1039/c3cp52981a

www.rsc.org/pccp

Resonant inelastic X-ray scattering and high-resolution X-ray absorption spectroscopy were used to identify the chemical state of a Co electrocatalyst *in situ* during the oxygen evolution reaction. After anodic electrodeposition onto Au(111) from a Co^{2+}-containing electrolyte, the chemical environment of Co can be identified to be almost identical to CoOOH. With increasing potentials, a subtle increase of the Co oxidation state is observed, indicating a non-stoichiometric composition of the working OER catalyst containing a small fraction of Co^{4+} sites. In order to confirm this interpretation, we used density functional theory with a Hubbard-*U* correction approach to compute X-ray absorption spectra of model compounds, which agree well with the experimental spectra. *In situ* monitoring of catalyst local structure and bonding is essential in the development of structure–activity relationships that can guide the discovery of efficient and earth abundant water splitting catalysts.

Introduction

The large-scale implementation of renewable energy use could be greatly facilitated with solar-to-fuel conversion processes that allow large amounts of energy to be stored, transferred and used in a fashion that is compatible with existing fuel-burning infrastructure, especially road transportation.[1] Such a photo-electrochemical conversion can involve, in its cathode reaction, either the reduction of CO_2, or of protons to hydrogen gas. Any of these conversions require a counter-electrode where water is oxidized in the oxygen evolution reaction (OER):

$$2H_2O \rightarrow 4H^+ + 4e^- + O_2 \text{ (in acid) or}$$
$$4OH^- \rightarrow 2H_2O + 4e^- + O_2 \text{ (in base)}$$

High OER overpotential and lack of stability of most electrode materials under harsh oxidizing conditions limit the practicability of electrochemical water splitting. For a more systematic approach towards the discovery of new catalyst materials, a fundamental understanding of electronic structure–activity relationships is needed. For transition metal electrocatalysts, the d-band model has been shown to predict very reliably the activity of electrocatalysts for hydrogen oxidation (HOR) and oxygen reduction (ORR) reactions in fuel cells.[2–4] In these cases, however, the catalyst is assumed to be in the metallic state. Conversely, by far most catalyst materials for OER, even noble metals, will form oxides at the high potentials needed to oxidize water. Oxides of Ru and Ir have been reported to be the best OER catalysts in acid and base, respectively.[5] While a volcano relationship has been reported[6–9] to predict the OER overpotential as function of the difference between binding energies of chemisorbed O and OH on a large number of metal oxide model structures, more experimental evidence is needed to identify the oxidation state and coordination environment in the electrocatalyst under working OER conditions.

Co oxide is among the most promising earth-abundant materials[10–14] but still has significantly higher overpotential than IrO_2, and there have been inconsistent reports as to which oxide species is the active OER catalyst. Most importantly, traditional "*ex situ*" analysis of catalyst materials might not reveal the structure and electronic properties under OER operating conditions, where the high electrochemical potential may drive the catalyst to a chemical state that is not stable without such an applied potential. Therefore, it is necessary to obtain information *operando* while the catalytic reaction is proceeding.

[a] *Joint Center for Artificial Photosynthesis, Lawrence Berkeley National Laboratory, Berkeley, CA 94720, USA. E-mail: dfriebel@slac.stanford.edu*
[b] *SUNCAT Center for Interface Science and Catalysis, SLAC National Accelerator Laboratory, Menlo Park, CA 94025, USA*
[c] *Department of Chemical and Biomolecular Engineering, University of California at Berkeley, Berkeley, CA 94720, USA*
[d] *Stanford Synchrotron Radiation Lightsource, SLAC National Accelerator Laboratory, Menlo Park, CA 94025, USA*
[e] *Linac Coherent Lightsource, SLAC National Accelerator Laboratory, Menlo Park, CA 94025, USA*

† Electronic supplementary information (ESI) available. See DOI: 10.1039/c3cp52981a

Here, we use *operando* X-ray absorption spectroscopy (XAS) to probe the electronic structure of an electrodeposited thin-layer Co oxide catalyst under OER conditions in alkaline NaOH electrolyte.

In order to enhance the sensitivity of XAS as an electronic structure probe, we employed the high energy resolution fluorescence detection (HERFD) mode, in which the lifetime broadening is experimentally reduced and more detailed spectral features can be observed than with conventional X-ray absorption near-edge structure (XANES).[15–20] In particular, the weak 1s → 3d transitions in the ''pre-edge'' region, which provide important information on spin state, oxidation state and coordination geometry,[21] are better resolved and less difficult to separate from the main absorption edge than in XANES.[16,22,23]

In addition to HERFD XAS, we also measured full $1s2p_{3/2}$ resonant inelastic X-ray scattering (RIXS) planes for a subset of samples. RIXS captures all $K\alpha_1$ decay channels instead of the narrow subset chosen in HERFD XAS. This is important in measurements of the pre-edge 1s → 3d transitions in which the interpretation of HERFD XAS as ''absorption spectrum'', due to strong final state interactions, may be incorrect.[24] Finally, we compare the measured HERFD XAS to theoretical XA spectra of several Co oxides obtained in density functional theory with Hubbard-*U* correction (DFT + *U*). The pre-edge part of the computed absorption spectrum is used to identify the character of observed transitions.

A related electrocatalytic system was recently studied by Kanan *et al.* using a similar *operando* XAS approach but with conventional fluorescence detection.[25] In their work, a water oxidation catalyst was formed electrochemically from Co^{2+}-containing phosphate buffer, which at the same time served as the OER working electrolyte. Using neutral electrolyte in photoelectrochemical water splitting devices might at first glance appear advantageous over the harsh acidic or alkaline conditions in current state-of-the-art electrolyzers. However, the low ionic conductivity of neutral electrolytes limits performance and will eventually, even in buffered solutions, lead to the buildup of pH gradients. In particular the OER catalyst would experience a local pH decrease which is detrimental to a large number of earth-abundant transition metal oxides with reasonable OER activity including Co oxides. Conversely, most of these oxides are stable under alkaline conditions. In the case of Co studied here, it is important to note that the solubility of Co^{2+} at pH = 13 is reduced by 12 orders of magnitude compared to the conditions employed by Kanan *et al.*[25] This difference strongly affects the chemical state of Co under alkaline OER conditions due to kinetic hindrance of phase transformations that is not reflected in Pourbaix diagrams[26] and cannot be accurately predicted from the previous measurements at neutral pH.

Experimental section

Sample preparation

Co oxide electrodeposition electrolyte, 0.01 M $Co(NO_3)_2$ + 0.1 M $NaCH_3CO_2$, was made from $Co(NO_3)_2{\cdot}6H_2O$ (99%, Aldrich) and 0.1 M $NaCH_3CO_2{\cdot}3H_2O$ (99%, EMD) with ultrapure water (Millipore Gradient™); $NaOH{\cdot}H_2O$ (EMD Suprapur®) was used to make the 0.1 M NaOH working electrolyte.

A 4 mm diameter commercial Au(111) single-crystal (MaTeck, Jülich, Germany) was cleaned by electrochemical oxidation (+10 V *vs.* Pt counter electrode in 0.05 M H_2SO_4) to remove any possible metal impurities, and was subsequently flame-annealed with a butane torch and allowed to cool down under N_2 atmosphere. The polished face of the crystal was then immersed to form a hanging meniscus with the Co oxide deposition electrolyte. Co oxide was galvanostatically deposited using an anodic current density of 0.1 mA cm^{-2} for 75 s, resulting in an approximately 30 nm thick Co oxide layer. The sample was then rinsed with ultrapure water and mounted in the electrochemical *in situ* hanging meniscus cell,[20] which provides a three-electrode setup with Pt counter and Pt pseudo-reference electrodes. All potentials measured in the 0.1 M NaOH working electrolyte were converted to values with respect to the reversible hydrogen electrode (RHE).

X-ray spectroscopy

All *in situ* HERFD XAS and RIXS measurements were carried out at the Stanford Synchrotron Radiation Lightsource (SSRL) using the high-resolution spectrometer at beamline 6-2.[27] The incident energy was selected using a Si(311) double-crystal monochromator; a Rowland circle spectrometer (R = 1 m) consisting of three spherically bent Si(531) perfect crystals was aligned to the peak of the Co $K\alpha_1$ emission line at 6930.3 eV, corresponding to a Bragg angle of 77.02°. HERFD XAS scans were collected with the emission energy fixed at this position. RIXS planes were collected by stepping the spectrometer through 64 different positions between Bragg angles of 77.39° and 76.82° corresponding to emission energies of 6920.25 eV and 6936.0 eV, respectively. The combined resolution of monochromator and analyzer was determined to be ~0.5 eV.

Computational methods

K-edge absorption spectra of Co oxides were calculated using parameter-free density functional theory with a Hubbard-*U* correction (DFT + *U*) method. In order to obtain X-ray absorption spectra, the charge density was calculated in self-consistent manner using the PW package of Quantum-Espresso.[28] The absorption spectrum was then computed *via* the continued fraction method as implemented in XSPECTRA package.[29–31] Since norm-conserving pseudo-potentials (PPs) require large cutoffs, we used ultrasoft PPs[29] with two projectors per channel and PPs of Co and O having also nonlinear core corrections.[30] The use of ultrasoft PPs allows for an only modest plane wave cutoff of 50 Ry. In addition, spin-polarized Perdew–Burke–Ernzerhof[31] parameterization of the generalized gradient approximation of DFT was employed. In a previous XAS study of $LiCoO_2$,[32] the Hubbard-*U* parameter was found to be essential in order to reproduce the electronic properties as well as the XA spectrum of the compound. The value of the effective *U* parameter applied to d-electrons of Co was determined self-consistently using the linear response approach[33] as U_{eff} = 5.6 eV. Since we use the PPs identical to those used in the study of

Table 1 Description of the crystallographic structures under study and further computational details of the XANES calculations. The point group of the absorbing atom site is indicated in brackets

Compound	Structure type	Space group	Cell parameters [Å]	Absorber atom sites	Supercell
CoO [36]	Rocksalt	$Fm\bar{3}m$	a = 4.263	Co^{2+} ($\bar{3}m$)	Cubic, 4 × 4 × 4 (64 atoms)
Co_3O_4 [37]	Spinel	$Fd\bar{3}m$	a = 8.08	Co^{2+} ($\bar{4}3m$) Co^{3+} ($\bar{3}m$)	Cubic, 2 × 2 × 2 (56 atoms)
β-CoOOH [38]	Layered	$R\bar{3}m$	a = 2.851, c = 13.150	Co^{3+} ($\bar{3}m$)	Hex, 3 × 3 × 1 (108 atoms)
β-$H_{0.5}CoO_2$	Layered	$R\bar{3}m$	a = 2.855, c = 13.262	Co^{3+}, Co^{+4} ($\bar{3}m$)	Hex, 4 × 4 × 1 (168 atoms)

$LiCoO_2$,[34] the same value was adopted in this work for all Co oxide phases.

Each spectrum was obtained from a supercell calculation (see Table 1), for which one core–hole was placed in the position of an absorbing atom. The core–hole is represented by a pseudo-potential with only one 1s electron in its electronic configuration and treated within the gauge-including projector augmented-wave approach.[35] While only the Γ point is used to obtain charge density, a 4 × 4 × 4 k-point Monkhorst–Pack mesh grid and 1.5 eV broadening were used for the XAS continued fraction calculation at the Co K-edge (0.5 eV for pre-edge). For all oxides, we use experimental crystal structures, with the exception of β-$H_{0.5}CoO_2$. The structure of β-$H_{0.5}CoO_2$ was obtained from β-CoOOH by removal of half of the protons and subsequent relaxation of the remaining atoms in the hexagonal crystalline lattice. The structural parameters are also given in Table 1.

The isotropic spectra were calculated for either octahedral Co absorption sites with D_{3d} ($\bar{3}m$) point-group symmetry or for tetrahedral Co absorption sites with T_d ($\bar{4}3m$) point-group symmetry. Following the procedure described in ref. 32, 39 and 40 the dipole isotopic spectra are given as

$$\sigma_{iso}^{D} = (\sigma_{xx} + \sigma_{yy} + \sigma_{zz})/3,$$

where σ_{xx}, σ_{yy}, σ_{zz} are the electric dipole absorption spectra calculated along three perpendicular directions. Due to symmetry, $\sigma_{xx} = \sigma_{yy} = \sigma_{zz}$ for cubic and $\sigma_{xx} = \sigma_{yy}$ for hexagonal systems. To extract the isotropic quadrupole cross-section, we use expressions from ref. 34 and 40 for cubic and hexagonal systems, respectively. The above expressions are strictly true only for ideal crystal structures. Considering additional absorber sites due to symmetry distortions as in case of ref. 34 leads to only small corrections in the spectra and it is neglected here. This is also the case for β-$H_{0.5}CoO_2$ for which the Co site in the relaxed atomic structure has only approximate D_{3d} ($\bar{3}m$) point-group symmetry.

Results and discussion

RIXS planes of standard compounds

In order to identify the chemical nature of the electrodeposited Co oxide film on Au(111), we recorded full RIXS planes *in situ* in 0.1 M NaOH electrolyte at four different potentials. In addition, RIXS planes of well-defined standard compounds were obtained. Fig. 1 shows RIXS planes of the pre-edge region of the standards CoO, Co_3O_4 and CoOOH. The first two compounds both contain Co^{2+} ions, which can be clearly seen to give rise to a complex multiplet structure due to their $3d^7$ configuration with half-filled orbitals. Furthermore, 2p–3d interactions in the final state cause at least one of the pre-edge resonances in each Co^{2+}-containing compound to be shifted from the diagonal of the RIXS plane. By contrast, CoOOH exhibits only one sharp resonance due to local 1s → 3d transitions and, in addition, a broad feature at higher energy which is characteristic for non-local transitions involving 3d states from Co atoms surrounding the absorber atom.[22,41,42] All pre-edge resonances in CoOOH lie on the diagonal of the RIXS plane and can thus be captured already with HERFD XAS.

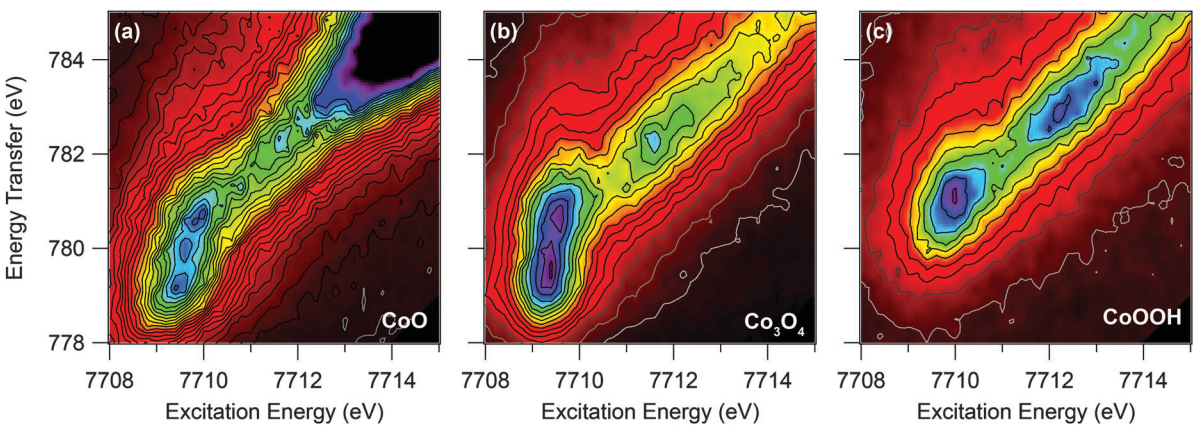

Fig. 1 RIXS planes map the 1s → 3d X-ray absorption features of the standards (a) CoO, (b) Co_3O_4 and (c) CoOOH. For CoO in (a), the onset of the much more intense 1s → 4p transitions at excitation energies greater than 7713 eV can also be seen. Intensities are shown with a color scale ranging from deep red (low) to deep purple (high).

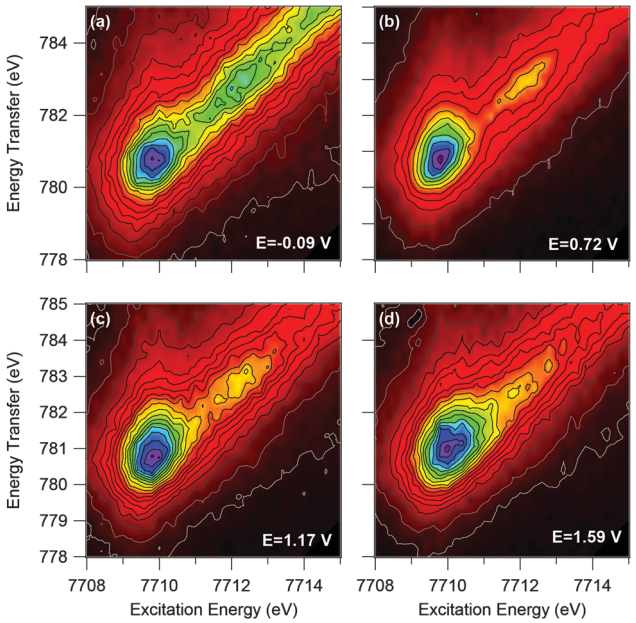

Fig. 2 *In situ* RIXS planes of the Co oxide/Au(111) electrocatalyst at four different potentials, (a) −0.09 V, (b) 0.72 V, (c) 1.17 V and (d) 1.59 V. Visible formation of O_2 bubbles was taking place during acquisition of the RIXS plane in (d).

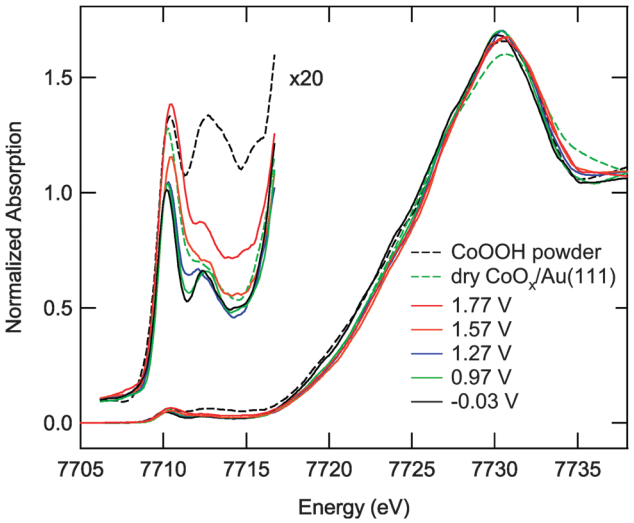

Fig. 3 *In situ* HERFD XAS of Co oxide/Au(111) electrocatalyst as function of potential. Also shown are the spectra of the dry, as-prepared Co/Au(111) sample and, for reference, CoOOH powder.

Comparison with *in situ* RIXS during OER

In situ RIXS planes of the Co oxide/Au(111) electrocatalyst at four different potentials (Fig. 2) all show similarity with that of CoOOH over a wide potential range in that off-diagonal resonances are completely absent, and the pre-edge region can be largely described with the same two local and non-local resonances as in CoOOH. However, the non-local resonance is notably weaker and there are subtle changes of the relative peak intensities and positions with increasing potential, which will be discussed in more detail by means of the *in situ* HERFD XA spectra in the following section. We propose that the relatively weak non-local resonance in the electrodeposited film is caused by a polarization effect due to epitaxial growth of CoOOH(0001)/Au(111).

In situ HERFD XAS

Due to the slow data acquisition in RIXS, the accessible potential range is somewhat limited since O_2 bubble formation at high OER currents alters the X-ray transmission through the electrolyte and thereby the fluorescence intensity from the working electrode in an unpredictable fashion. In order to assess the potential-induced changes in detail, HERFD XAS measurements were carried out for a larger number of electrochemical potentials (Fig. 3), including conditions of high OER current density. The much faster data acquisition in HERFD XAS circumvents the aforementioned problems with bubble formation.

At low potentials, the pre-edge region shows two distinguishable features, a sharp peak at 7710.2 eV and a much broader peak at 7712.5 eV, which can be assigned to local and non-local transitions of high-spin Co^{3+} in an octahedral environment.[22,41,42]

As the potential is increased towards OER conditions, the peak at lower energy appears to broaden towards high energy and increase its overall intensity. Concurrently, the main absorption edge shifts to higher energy, indicating an increase in the average Co oxidation state. In order to follow the changes in the pre-edge region in more detail, we performed least-squares fits using three pseudo-Voigt profiles and a sigmoid function for the onset of the main absorption edge. The strong similarity of the main-edge absorption and multiple-scattering features, aside from the small shift of the edge position, leads us to assume that the species observed at the lowest potential remains present throughout the experiment. Therefore, we keep the positions and widths of the peaks at 7710.2 eV and 7712.5 eV fixed. A third peak at 7710.9 eV is then necessary to fit all spectra at higher potentials (Fig. 4). We propose that the third peak is a contribution from Co^{4+} ions in $H_{1-x}CoO_2$; this is consistent with the shift of the main absorption edge to higher energy.

HERFD XAS theory

First-principles calculations of XA spectra clearly confirm our interpretation of the experimental HERFD XAS results. In Fig. 5, we compare calculated XA spectra of CoO, Co_3O_4 and CoOOH standards and of a hypothetical $H_{0.5}CoO_2$ system to the measured HERFD XAS results. The first observation from Fig. 5 is that using the DFT + U computational methodology results in very good agreement of the calculated spectra of the standard compounds with the measured data, especially for the strong Co 1s → 4p resonance and the multiple-scattering features above the main absorption edge. Second, using a constant energy shift of 7710 eV relative to the Fermi level for the computed spectra also reproduces the position of the experimental main absorption edges. As we have already discussed, this shift to higher energies strongly correlates with the increase of the average Co oxidation state. Based on these findings, we

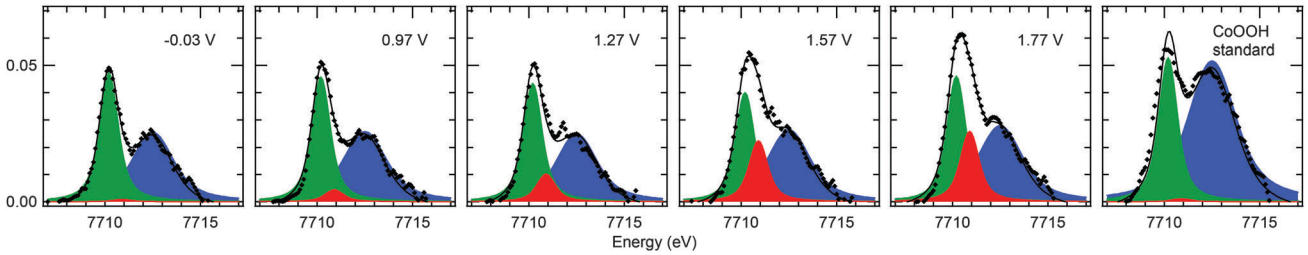

Fig. 4 HERFD XAS pre-edge features after subtraction of the main-edge. Measured data and fit results are shown as markers and solid lines, respectively. The peak components are shown as colored areas.

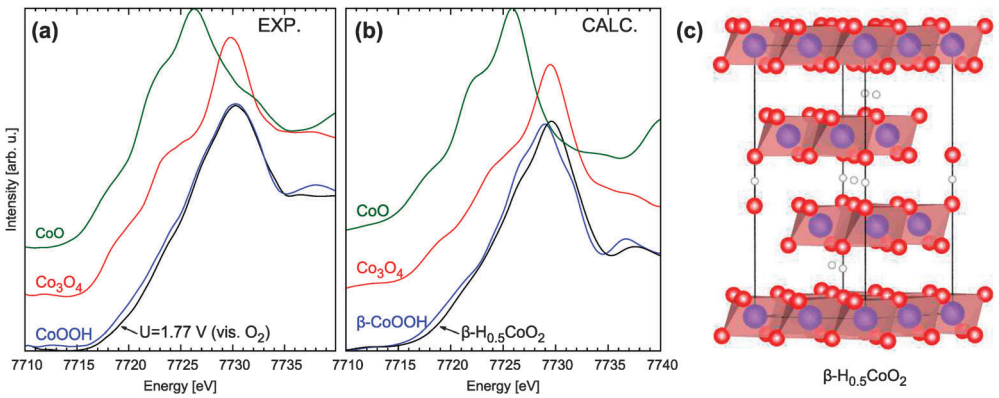

Fig. 5 (a) Experimental HERFD XAS of powdered Co oxide reference compounds. Also shown is the Co oxide/Au(111) sample at U = 1.77 V *vs.* RHE (black) during visible O_2 generation. (b) Theoretical XAS calculations using only the dipole cross-section for the same reference compounds as in (a), and for the optimized structure of β-$H_{0.5}CoO_2$ (see also Table 1 for computational details). Each computed spectrum was shifted by a constant of 7010 eV relative to its Fermi level. The broadening parameter was set to 1.5 eV in the continued fraction algorithm. (c) Optimized β-$H_{0.5}CoO_2$ structure.

feel confident in predicting the spectrum of a hypothetical $H_{0.5}CoO_2$ compound. When compared directly to CoOOH in Fig. 5b, we see a small shift of the main-edge of $H_{0.5}CoO_2$ to higher energies, indicating the presence of Co^{4+}. Almost the same shift is present in the Co oxide/Au(111) sample under applied voltage with visible formation of O_2 bubbles. Moreover, the overall shape of the $H_{0.5}CoO_2$ spectrum is similar to that of the Co oxide/Au(111) sample. Finally, we also calculated the XA spectra for α-$NaCoO_2$ and β/γ-$Na_{0.5}CoO_2$ in order to assess whether Na cation intercalation might occur, as has been proposed elsewhere (ESI†).[37,43] However, by far the closest agreement of the spectral shape with the Co oxide/Au(111) sample under OER operating conditions was found for the $H_{0.5}CoO_2$ system.

Pre-edge. The comparison of the pre-edge peaks is shown in Fig. 6. Similar to our experimental data, the calculation for CoOOH gives a sharp feature and, *ca.* 2 eV above, a much broader peak. Following the example of Juhin *et al.* who studied the pre-edge of structurally and electronically similar $LiCoO_2$,[40] we can separate the pre-edge features into contributions due to dipole and quadrupole transitions and their polarization dependence. It can be clearly seen that the sharper peak at lower energy purely originates from quadrupole transitions into unoccupied e_g states, which is not too surprising since all t_{2g} states are filled for low-spin octahedral Co^{3+}. The broader feature at higher energy is a dipole transition into 4p states of the Co absorber atom that are hybridized with O 2p states, and with 3d states of a neighboring Co atom. The latter feature is significantly weakened when the electric field vector of the incident X-rays is oriented perpendicular to the *c*-axis of layered compounds. The markedly weaker intensity of the non-local pre-edge transition in CoOOH–Au(111) compared to the powdered CoOOH standard can therefore be explained with a polarization effect caused by a preferential epitaxial orientation of the electrodeposited CoOOH film with its *c*-axis parallel to the Au(111) surface normal. This is plausible given the matching 3-fold symmetries and the small (<1%) mismatch between the in-plane lattice constants of Au(111) and CoOOH(001) planes.

While we use the same approach for XAS calculations of materials containing Co^{2+} or Co^{4+}, we caution that the DFT-based approach neglects multi-electronic interactions that lead to additional multiplet structure of the transitions into the partially filled Co 3d states, which is absent only in the special case of octahedral low-spin Co^{3+}. However, with limited instrumental resolution, RIXS can only partially resolve the multiplet structure, resulting in an ''incomplete'' fine structure somewhere in between the full multiplet splitting and the more simple single-electron picture provided by DFT; the latter can therefore still be useful as a guide in the interpretation of pre-edge features. Based on the calculated pre-edge peaks (shown in Fig. 6.), we observe that for each standard, DFT + U theory is

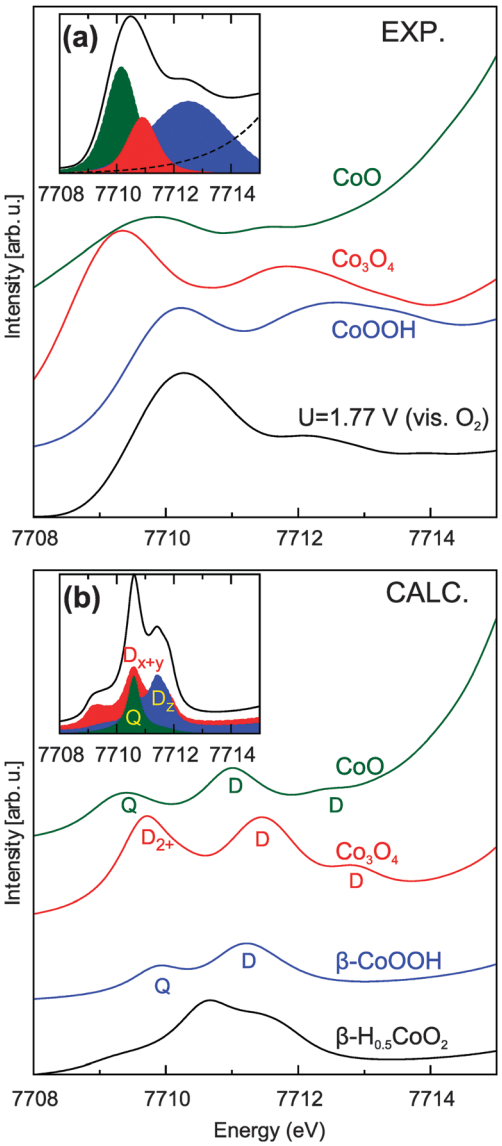

Fig. 6 (a) Experimental HERFD XAS pre-edge features of the same oxides as in Fig. 5. (b) Theoretical XAS pre-edges for the corresponding ideal crystalline systems with dipole (D) and quadrupole (Q) contributions to the cross-section (see also Table 1 for computational details). Each computed spectrum was shifted by a constant of 7009 eV relative to its Fermi level. The broadening parameter was set to 0.5 eV in the continued fraction algorithm (0.25 eV in the inset). The insets show (a) the pre-edge components of H_xCoO_2/Au(111) measured at U = 1.77 V (from Fig. 4, dashed line: fitted main-edge contribution) compared to the components of β-$H_{0.5}CoO_2$ pre-edge (b).

in reasonable qualitative agreement with the experiment, *i.e.* relative positions and origin of the peaks, while quantitative agreement is much more difficult to achieve. For CoO and Co_3O_4, some of the calculated pre-edge features appear to be missing in the measured HERFD XAS. We note that this apparent discrepancy is not an error, but rather results from the shift of these features to lower energy transfers, as can be seen in the full RIXS planes of these compounds in Fig. 1. While the theory, within the limitations of its single-electron approach, captures all transitions from the ground state into 1s core–hole excited intermediate states, HERFD XAS will not or only partially reveal those intermediate states that are in off-diagonal positions in RIXS. However, the pre-edge spectrum of $H_{0.5}CoO_2$ offers a qualitative explanation for the origin of the potential-induced changes of the pre-edge features in Co oxide/Au(111).

We conclude that the new feature at high potentials that arises at 7710.9 eV in addition to the two CoOOH features is the strongest pre-edge feature of Co^{4+} in a non-stoichiometric H_xCoO_2 ($x < 1$) phase, while its multiplet structure cannot be resolved due to the relatively weak intensities of its peaks and the overall small concentration of Co^{4+} in a Co^{3+} matrix. It is important to note that the subtle changes of the pre-edge structure shown here would be almost impossible to observe in a conventional XAS experiment, which suffers from higher effective core–hole lifetime broadening and a much stronger overlap between pre-edge and main-edge regions. In fact, a previous *in situ* XAS study of $Co(OH)_2$ on polycrystalline Au substrates found highly irreversible oxidation of $Co(OH)_2$ to CoOOH where the latter exhibited hardly any oxidation state changes.[44] The difference to the results shown here can be explained on one hand with the different spectral resolution and, on the other hand, with the more limited potential range in the previous work, which did not include the potential region of oxygen evolution.

The local structure of the H_xCoO_2 catalyst studied here is similar to that observed by Kanan *et al.* in a phosphate buffer electrolyte.[25] However, the amount by which the Co^{3+} oxidation state is exceeded appears much higher in phosphate buffer than in the much more alkaline electrolyte used here. To explain this difference, we propose that the particularly small size of cobaltate clusters, which was observed with EXAFS[25] and high energy X-ray scattering,[45] allows for higher structural flexibility and improved exchange of protons in the transformation between CoOOH and H_xCoO_2. The small cluster size at pH = 7 originates from a dynamic equilibrium between insoluble Co^{3+} species and hydrated Co^{2+} ions in the electrolyte.[12,25] At the higher pH used here, the solubility of Co^{2+} is reduced by 12 orders of magnitude;[26] therefore, we conjecture that much larger aggregates of H_xCoO_2 are formed and that the extent of Co^{4+} formation is more limited. While the exact process by which H_xCoO_2 is formed is not known, we propose that it may involve anodic oxidation of CoOOH by OH^- *via* the reaction $CoOOH + (1-x)OH^- \rightarrow H_xCoO_2 + (1-x)H_2O + (1-x)e^-$ under highly alkaline conditions.

We note that the gradually increasing amount of Co^{4+} sites with overpotential under OER operating conditions may be contributing to the limited catalytic performance. A more detailed theoretical study using the DTF + U approach[46] indicates that the adsorption energy of OH is much closer to the optimum value when it is bound to a Co^{3+} site than at a Co^{4+} site, and that the difference results in 0.32 V higher overpotential when the Co^{4+}–OH intermediate is involved. Therefore, controlling the metal oxidation state is an important design criterion for OER catalysts. To a limited extent, this can already be achieved by the variation of the electrolyte pH, where higher pH results in larger cobaltate aggregates where Co^{4+}

formation is kinetically hindered by the more limited transport of protons. However, since such a kinetic hindrance may not persist during prolonged operation and the pH also strongly affects electrolyte resistance, we propose instead the substitution of Co sites in CoOOH with suitable dopants as a more robust means of tuning the stability of different Co oxidation states. *In situ* X-ray absorption spectroscopy provides the probe that is needed to monitor this design criterion under catalytic operating conditions.

Acknowledgements

This material is based upon work performed by the Joint Center for Artificial Photosynthesis, a DOE Energy Innovation Hub, supported through the Office of Science of the U.S. Department of Energy under Award Number DE-SC0004993. This research was partly carried out at the Stanford Synchrotron Radiation Lightsource, a National User Facility operated by Stanford University on behalf of the U.S. Department of Energy, Office of Basic Energy Sciences. D.F. would like to thank Uwe Bergmann for useful discussions. M.B. would like to thank Amélie Juhin for helpful discussions concerning calculations of the theoretical spectra.

References

1 M. G. Walter, E. L. Warren, J. R. McKone, S. W. Boettcher, Q. Mi, E. A. Santori and N. S. Lewis, *Chem. Rev.*, 2010, **110**, 6446–6473.
2 J. Greeley, T. F. Jaramillo, J. Bonde, I. B. Chorkendorff and J. K. Nørskov, *Nat. Mater.*, 2006, **5**, 909–913.
3 J. K. Nørskov, J. Rossmeisl, A. Logadottir, L. Lindqvist, J. R. Kitchin, T. Bligaard and H. Jónsson, *J. Phys. Chem. B*, 2004, **108**, 17886–17892.
4 J. Greeley, I. E. L. Stephens, A. S. Bondarenko, T. P. Johansson, H. A. Hansen, T. F. Jaramillo, J. Rossmeisl, I. Chorkendorff and J. K. Nørskov, *Nat. Chem.*, 2009, **1**, 552–556.
5 S. Trasatti, *Electrochim. Acta*, 1984, **29**, 1503–1512.
6 M. García-Mota, A. Vojvodic, H. Metiu, I. C. Man, H.-Y. Su, J. Rossmeisl and J. K. Nørskov, *ChemCatChem*, 2011, **3**, 1607–1611.
7 I. C. Man, H.-Y. Su, F. Calle-Vallejo, H. A. Hansen, J. I. Martínez, N. G. Inoglu, J. Kitchin, T. F. Jaramillo, J. K. Nørskov and J. Rossmeisl, *ChemCatChem*, 2011, **3**, 1159–1165.
8 J. Suntivich, K. J. May, H. A. Gasteiger, J. B. Goodenough and Y. Shao-Horn, *Science*, 2011, **334**, 1383–1385.
9 A. Vojvodic and J. K. Nørskov, *Science*, 2011, **334**, 1355–1356.
10 F. Jiao and H. Frei, *Angew. Chem., Int. Ed.*, 2009, **48**, 1841–1844.
11 A. J. Esswein, M. J. McMurdo, P. N. Ross, A. T. Bell and T. D. Tilley, *J. Phys. Chem. C*, 2009, **113**, 15068–15072.
12 M. W. Kanan and D. G. Nocera, *Science*, 2008, **321**, 1072–1075.
13 B. Marsan, N. Fradette and G. Beaudoin, *J. Electrochem. Soc.*, 1992, **139**, 1889–1896.
14 B. S. Yeo and A. T. Bell, *J. Am. Chem. Soc.*, 2011, **133**, 5587–5593.
15 F. M. F. de Groot, M. H. Krisch and J. Vogel, *Phys. Rev. B: Condens. Matter Mater. Phys.*, 2002, **66**, 195112.
16 K. Hämäläinen, D. P. Siddons, J. B. Hastings and L. E. Berman, *Phys. Rev. Lett.*, 1991, **67**, 2850–2853.
17 O. V. Safonova, M. Tromp, J. A. van Bokhoven, F. M. F. de Groot, J. Evans and P. Glatzel, *J. Phys. Chem. B*, 2006, **110**, 16162–16164.
18 D. Friebel, D. J. Miller, D. Nordlund, H. Ogasawara and A. Nilsson, *Angew. Chem., Int. Ed.*, 2011, **50**, 10190–10192.
19 D. Friebel, D. J. Miller, C. P. O'Grady, T. Anniyev, J. Bargar, U. Bergmann, H. Ogasawara, K. T. Wikfeldt, L. G. M. Pettersson and A. Nilsson, *Phys. Chem. Chem. Phys.*, 2011, **13**, 262–266.
20 D. Friebel, V. Viswanathan, D. J. Miller, T. Anniyev, H. Ogasawara, A. H. Larsen, C. P. O'Grady, J. K. Nørskov and A. Nilsson, *J. Am. Chem. Soc.*, 2012, **134**, 9664–9671.
21 T. E. Westre, P. Kennepohl, J. G. DeWitt, B. Hedman, K. O. Hodgson and E. I. Solomon, *J. Am. Chem. Soc.*, 1997, **119**, 6297–6314.
22 W. M. Heijboer, P. Glatzel, K. R. Sawant, R. F. Lobo, U. Bergmann, R. A. Barrea, D. C. Koningsberger, B. M. Weckhuysen and F. M. F. de Groot, *J. Phys. Chem. B*, 2004, **108**, 10002–10011.
23 P. Glatzel and U. Bergmann, *Coord. Chem. Rev.*, 2005, **249**, 65–95.
24 P. Glatzel, T.-C. Weng, K. Kvashnina, J. Swarbrick, M. Sikora, E. Gallo, N. Smolentsev and R. A. Mori, *J. Electron Spectrosc. Relat. Phenom.*, 2013, **188**, 17–25.
25 M. W. Kanan, J. Yano, Y. Surendranath, M. Dincă, V. K. Yachandra and D. G. Nocera, *J. Am. Chem. Soc.*, 2010, **132**, 13692–13701.
26 J. Chivot, L. Mendoza, C. Mansour, T. Pauporté and M. Cassir, *Corros. Sci.*, 2008, **50**, 62–69.
27 D. Sokaras, T.-C. Weng, D. Nordlund, R. Alonso-Mori, P. Velikov, D. Wenger, A. Garachtchenko, M. George, V. Borzenets, B. Johnson, T. Rabedeau and U. Bergmann, *Rev. Sci. Instrum.*, 2013, **84**, 053102.
28 P. Giannozzi, S. Baroni, N. Bonini, M. Calandra, R. Car, C. Cavazzoni, D. Ceresoli, G. L. Chiarotti, M. Cococcioni, I. Dabo, A. D. Corso, S. de Gironcoli, S. Fabris, G. Fratesi, R. Gebauer, U. Gerstmann, C. Gougoussis, A. Kokalj, M. Lazzeri, L. Martin-Samos, N. Marzari, F. Mauri, R. Mazzarello, S. Paolini, A. Pasquarello, L. Paulatto, C. Sbraccia, S. Scandolo, G. Sclauzero, A. P. Seitsonen, A. Smogunov, P. Umari and R. M. Wentzcovitch, *J. Phys.: Condens. Matter*, 2009, **21**, 395502.
29 D. Vanderbilt, *Phys. Rev. B: Condens. Matter Mater. Phys.*, 1990, **41**, 7892–7895.
30 S. G. Louie, S. Froyen and M. L. Cohen, *Phys. Rev. B: Condens. Matter Mater. Phys.*, 1982, **26**, 1738–1742.
31 J. P. Perdew, K. Burke and M. Ernzerhof, *Phys. Rev. Lett.*, 1996, **77**, 3865–3868.
32 C. Brouder, A. Juhin, A. Bordage and M.-A. Arrio, *J. Phys.: Condens. Matter*, 2008, **20**, 455205.

33 M. Cococcioni and S. de Gironcoli, *Phys. Rev. B: Condens. Matter Mater. Phys.*, 2005, **71**, 035105.
34 A. Juhin, C. Brouder, M.-A. Arrio, D. Cabaret, P. Sainctavit, E. Balan, A. Bordage, A. P. Seitsonen, G. Calas, S. G. Eeckhout and P. Glatzel, *Phys. Rev. B: Condens. Matter Mater. Phys.*, 2008, **78**, 195103.
35 C. J. Pickard and F. Mauri, *Phys. Rev. B: Condens. Matter Mater. Phys.*, 2001, **63**, 245101.
36 R. Ma, Z. Liu, K. Takada, K. Fukuda, Y. Ebina, Y. Bando and T. Sasaki, *Inorg. Chem.*, 2006, **45**, 3964–3969.
37 J. B. Gerken, J. G. McAlpin, J. Y. C. Chen, M. L. Rigsby, W. H. Casey, R. D. Britt and S. S. Stahl, *J. Am. Chem. Soc.*, 2011, **133**, 14431–14442.
38 R. G. Delaplane, J. A. Ibers, J. R. Ferraro and J. J. Rush, *J. Chem. Phys.*, 1969, **50**, 1920–1927.
39 C. Brouder, *J. Phys.: Condens. Matter*, 1990, **2**, 701.
40 A. Juhin, F. de Groot, G. Vankó, M. Calandra and C. Brouder, *Phys. Rev. B: Condens. Matter Mater. Phys.*, 2010, **81**, 115115.
41 F. M. F. de Groot, P. Glatzel, U. Bergmann, P. A. van Aken, R. A. Barrea, S. Klemme, M. Hävecker, A. Knop-Gericke, W. M. Heijboer and B. M. Weckhuysen, *J. Phys. Chem. B*, 2005, **109**, 20751–20762.
42 G. Vankó, F. M. F. de Groot, S. Huotari, R. J. Cava, T. Lorenz, M. Reuther, 2008, arXiv, 0802.2744.
43 M. Butel, L. Gautier and C. Delmas, *Solid State Ionics*, 1999, **122**, 271–284.
44 D. Totir, Y. Mo, S. Kim, M. R. Antonio and D. A. Scherson, *J. Electrochem. Soc.*, 2000, **147**, 4594–4597.
45 P. Du, O. Kokhan, K. W. Chapman, P. J. Chupas and D. M. Tiede, *J. Am. Chem. Soc.*, 2012, **134**, 11096–11099.
46 M. Bajdich, M. García-Mota, A. Vojvodic, J. K. Norskov and A. T. Bell, *J. Am. Chem. Soc.*, 2013, DOI: 10.1021/ja405997s.